PHYSICAL REVIEW C VOLUME 55, NUMBER 5 MAY 1997

Mapping the proton drip line up to $A = 70$

W. E. Ormand
Dipartimento di Fisica, Università Degli Studi di Milano, and Istituto Nazionale di Fisica Nucleare,
Sezione di Milano, Via Celoria 16, 20133 Milano, Italy;
Physics Division, Oak Ridge National Laboratory, P.O. Box 2008, MS-6373 Building 6003, Oak Ridge, Tennessee 37831-6373;
and Department of Physics and Astronomy, 202 Nicholson Hall, Louisiana State University, Baton Rouge, Louisiana 70803-4001

(Received 23 December 1996)

Coulomb energy differences between mirror nuclei with $A \leqslant 70$ are calculated within the framework of the nuclear shell model using an effective Coulomb plus isovector and isotensor interaction. Absolute binding energies for proton-rich nuclei are predicted by adding the calculated Coulomb shifts to experimentally measured binding energies for the neutron-rich mirror. The location of the proton drip line is investigated, as well as candidates for the exotic decay mode known as diproton emission. Taking into account the lifetimes of competing decay modes and limits imposed by experimental setups, it is concluded that the best candidates for the observation of correlated diproton emission are ^{45}Fe, ^{48}Ni, and ^{63}Se. [S0556-2813(97)06505-9]

PACS number(s): 21.10.Dr, 21.10.Sf, 21.10.Tg, 23.50.+z

I. INTRODUCTION

The structure of exotic nuclei, i.e., nuclei with extreme isospin values, is one of the most exciting challenges in low-energy nuclear physics today. Detailed theoretical studies of exotic nuclei, when confronted with experiments, will yield important information about the interaction between nucleons in the nucleus and the validity of our models for the structure of nuclei. In addition, the study of exotic nuclei is essential to many fundamental issues in physics today, in particular, the weak interaction and nuclear astrophysics. For example, it is believed that many of the heavy elements in the universe are produced by the radiative capture of neutrons (r process) [1] or protons (rp process) [2] on unstable nuclei. The competition between beta decay and particle capture traces out a path that synthesizes the known elements. The details of this path, and, hence, the abundance of the elements produced, depends on the temperature of the site, as well as explicit nuclear properties such as binding energies, level densities, spectroscopic factors, and beta-decay lifetimes.

An additional new feature of proton-rich nuclei that will be explored in the next few years is the possibility of a new decay mode known as diproton emission. Because of the pairing interaction, a nucleus with an even number of protons (Z,N) is generally more tightly bound than a $(Z-1,N)$ nucleus, but because of the symmetry energy and Coulomb repulsion, it may be unbound relative to the $(Z-2,N)$ system. The number of candidates for the observation of this decay mode, however, is sharply limited by the two-proton separation energy. This is in part due to the fact that β^+ emission is a competing decay mechanism, and because of the large Coulomb energy difference between the parent and daughter nuclei, the beta-decay lifetimes are of the order of 1–100 ms. In addition, a further constraint on the observation of diproton emission can be imposed by the experimental apparatus, since, in many experiments, the parent nucleus must live long enough to be identified. Generally speaking, these two practical constraints limit the observable lifetime for diproton decay to 10^{-8}–10^{-3} s. On the other hand, the decay rate for diproton emission is determined by the probability to penetrate through the Coulomb barrier, which, in turn, is exponentially dependent on the two-proton separation energy. As will be shown here, the number of candidates for which the observation of diproton decay is practical is limited to nuclei with two-proton separation energies between 0.9 and 1.4 MeV.

One of the principal motivations for the construction of radioactive beam facilities is to study the properties of nuclei near the limits of stability. Very few nuclei near the proton drip line have been identified, and the heaviest and most proton-rich nucleus observed to date is ^{49}Ni [3]. Even more difficult than the identification of an exotic nucleus is the measurement of its mass, and, at present, predictions regarding the r and rp processes must rely on theoretical estimates for nuclear binding energies.

Several methods have been used to obtain theoretical estimates for absolute binding energies. One is the liquid-drop formula and associated variants, such as the microscopic-macroscopic approach [4,5]. In general, these models are determined by fitting a set of liquid-drop parameters while including effects due to pairing and shell corrections to experimental data over a wide range of nuclei, and have been found to reproduce known nuclear masses at the level of approximately 800 keV (see, for example, Ref. [5]). Although the microscopic-macroscopic approach gives a good global description of nuclear binding energies and is the method of choice for heavy nuclei where detailed microscopic calculations are not feasible, there are notable discrepancies between experimental and calculated binding energies with neutron number between 20 and 40, as is illustrated in Fig. 1 of Ref. [5].

For lighter nuclei, however, more accurate binding energies can be achieved using the nuclear shell model, since, in many cases, it is necessary only to compute the Coulomb energy difference between mirror nuclei [6–8]. In this paper, Coulomb energy differences are computed for mirror nuclei in the fp shell for $46 \leqslant A \leqslant 70$. By then making use of experimental data for the neutron-rich members tabulated in Ref. [9], absolute binding energies are predicted with an estimated accuracy at the level of 50–200 keV. With these binding energies, two-proton separation energies are computed and rough estimates for the lifetimes for diproton decay are made. Given the practical constraints on the decay half-lives mentioned above, it is found that the best candidates for the experimental observation of correlated two-proton emission are ^{45}Fe, ^{48}Ni, and ^{63}Se.

This paper is organized into five sections. In Sec. II, the systematics of Coulomb energy differences between analog nuclei are discussed, while in Sec. III a shell-model description of these energy shifts is presented. Candidates for the exotic decay mode known as diproton emission are presented and analyzed in Sec. IV, and concluding remarks are collected in Sec. V.

II. SYSTEMATICS OF COULOMB ENERGY DIFFERENCES

If the nuclear Hamiltonian is composed of only one- and two-body parts, quite generally, it may be separated into three components. The dominant part, which is also responsible for most of the nuclear binding energy, is due to the strong interaction and is isoscalar in nature. The other two components are due to both the Coulomb interaction and charge-nonsymmetric parts of the nucleon-nucleon interaction, and are isovector and isotensor in character. If the isovector and isotensor components are weak relative to the isoscalar component, then the binding energies for the members of an isospin multiplet may be obtained within the context of the isobaric mass multiplet equation (IMME) [10–12]

$$\mathrm{BE}(A,T,T_z,i)=a(A,T,i)+b(A,T,i)T_z+c(A,T,i)T_z^2, \tag{1}$$

where T and $T_z=(Z-N)/2$ denote the isospin and its third component for the members of the isospin multiplet, and Z, N, and $A=Z+N$ are the number of protons, neutrons, and nucleons, respectively. The label i in Eq. (1) represents all other quantum numbers needed to denote the state, such as angular momentum, state number, etc. The coefficients a, b, and c separately depend on the isoscalar [13], isovector, and isotensor components of the nuclear Hamiltonian, respectively.

In shell-model calculations, the isoscalar part of the nuclear Hamiltonian is usually determined empirically by fitting to experimental binding energies and levels that have had the Coulomb energy subtracted off in an average way (cf. [14–16]). The predictive power of these effective Hamiltonians is indicated by the rms deviation between experimental data and calculated binding energies, and, to date, the best empirically determined Hamiltonian is that due to Wildenthal [14] for use in the $0d_{5/2}$, $0d_{3/2}$, and $1s_{1/2}$ orbitals, where the rms deviation between theory and experiment is of the order 200 keV. For the most part, this interaction may be thought of as indicative of the best accuracy that may be achieved within the framework of the nuclear shell model. For other model spaces, such as the fp shell (defined by the $0f_{7/2}$, $0f_{5/2}$, $1p_{3/2}$, and $1p_{1/2}$ orbitals), the effective shell-model Hamiltonian is less well determined and the deviation between theory and experiment is somewhat larger and is of the order 300 keV [16]. With this in mind, we must conclude that any attempt to compute absolute binding energies from first principles in the shell model would include an uncertainty of at least 200–300 keV in the a coefficient of Eq. (1).

From Eq. (1), the binding energy difference between iosbaric analogs with $T_z=\pm T$ is given by

$$\mathrm{BE}(A,T,T_z=T,i)-\mathrm{BE}(A,T,T_z=-T,i)=2b(A,T,i)T. \tag{2}$$

Therefore, the most accurate way to predict absolute binding energies for proton-rich nuclei whose analog has an experimentally measured mass is to compute the b coefficient for the multiplet (or the Coulomb energy difference) and add $2bT$ to the experimental binding energy $\mathrm{BE}_{\mathrm{expt}}(A,T,T_z=-T,i)$ of the neutron-rich analog. The overall uncertainty in the predicted binding energy is then of the order

$$\delta\mathrm{BE}(A,T,T_z=T,i) = \sqrt{(2\,\delta bT)^2+\delta(\mathrm{BE}_{\mathrm{expt}}(A,T,T_z=-T,i))^2}, \tag{3}$$

where δb is the uncertainty in the b coefficient and $\delta\mathrm{BE}_{\mathrm{expt}}(A,T,T_z=-T,i)$ is the uncertainty in the experimental binding energy. In many cases, it is possible to estimate the b coefficient with an uncertainty of the order of 30–40 keV [17], and, therefore, it may be possible to predict the binding energies of extreme proton-rich nuclei at the level of 100–200 keV.

In Refs. [6–8], the procedure outlined above was used to predict the absolute binding energies of nuclei with $36\leqslant A\leqslant 55$. Those three works approached Eq. (3) using slightly different methods, but with about the same level of accuracy, as is indicated by the overall agreement between them. In Ref. [6], Eq. (3) was evaluated using shell-model calculations for the pure $0f_{7/2}$-shell nuclei and a weak coupling approximation for those nuclei that spanned both the $0d_{3/2}$ and $0f_{7/2}$ orbits. In Ref. [7], all the Coulomb energy differences were evaluated within the framework of the shell model using the $0d_{3/2}$ and $0f_{7/2}$ orbits and an empirical isospin-nonconserving (INC) interaction [17]. Finally, in Ref. [8], Eq. (3) was evaluated using a method based on a parametrization of the Coulomb displacement energies [18]. The overall success of these works, and agreement between them, is essentially due to their empirical foundations. In each, a set of parameters was fit to experimental data, and the models were then extrapolated to predict the masses of unknown nuclei. This work is an extension of Ref. [7] in which absolute binding energies of proton-rich nuclei with $46\leqslant A\leqslant 70$ are predicted by computing the Coulomb displacements within the framework of the nuclear shell model.

Before continuing with the details and the results of the shell-model calculations, it is instructive to examine the systematic behavior of the Coulomb displacement energies. Indeed, one of the reasons for the success of the three different methods is the smooth behavior as a function of nucleon number A exhibited by experimental b coefficients. In addition, for a given mass number, the b coefficients are essentially constant to within 100 keV or so, as can be seen from Tables 3–7 in Ref. [17]. This behavior is easily understood from the liquid-drop model, where the Coulomb energy of a sphere of radius $R=r_0A^{1/3}$ with charge Ze is given by

$$E_C=\frac{3}{5}\frac{(Ze)^2}{R}. \tag{4}$$

The Coulomb energy difference between analog nuclei is then

$$\Delta E_C=\frac{3}{5}\frac{e^2}{R}\,[Z^2-(A-Z)^2]=\frac{3}{5}\frac{e^2}{R}\,A(Z-N) \tag{5}$$

$$=\frac{3}{5}\frac{e^2}{R}2AT=\frac{3}{5}\frac{e^2}{r_0}\,A^{2/3}(2T), \tag{6}$$

where $A=Z+N$ and the isospin is defined by $T=|Z-N|/2$. Hence, by comparing Eqs. (3) and (6), it is seen that the b coefficient is expected to increase as $A^{2/3}$.

For a comparison with experimental b coefficients, we turn to the more sophisticated liquid-drop parametrization of Ref. [5]. Here the form of the "Coulomb" energy will be outlined, and the Coulomb energy difference between analog nuclei will be evaluated using the parameters defined in Ref. [5]. In macroscopic models, the "Coulomb" contribution to the binding energy is [5]

$$E_{\mathrm{Coul}}=c_1\frac{Z^2}{A^{1/3}}\,B_3-c_4\frac{Z^{4/3}}{A^{1/3}}+f(k_fr_p)\frac{Z^2}{A}-c_a(N-Z), \tag{7}$$

where $c_1=3e^2/5r_0$ and $c_4=5/4(3/2\pi)^{2/3}c_1$. The first two terms in Eq. (7) are the direct and exchange Coulomb energies, the third is the proton form factor correction, and the last is the charge-asymmetry energy. The factor B_3 is the shape-dependent relative Coulomb energy, which, to leading order for a spherical shape, is given by

$$B_3=1-\frac{5}{y_0^2}+\frac{75}{8y_0^3}-\frac{105}{8y_0^5}, \tag{8}$$

with $y_0=(r_0/a_{\mathrm{den}})A^{1/3}\sim1.657A^{1/3}$. The proton form factor f is dependent on the Fermi wave number $k_f=(9\pi Z/4A)^{1/3}(1/r_0)$ and the proton rms radius $r_p=0.8$ fm (see Eq. (8) of Ref. [5]), and for nuclei with $A\sim50$ and $Z\sim A/2$ may be accurately approximated by $f=-0.214$ MeV. Using $r_0=1.16$ fm and $c_a=0.145$ MeV from Ref. [5], the b coefficient derived from the Coulomb energy difference between analog nuclei is

$$b_{\mathrm{LD}}=[0.7448A^{2/3}-1.882+1.535A^{-1/3}-0.7828A^{-1}]\ \mathrm{MeV}. \tag{9}$$

Shown in Fig. 1 is a comparison between Eq. (9) (solid line) and experimental b coefficients (solid squares). The experimental data comprise 116 b coefficients, and were taken from Tables 3–7 in Ref. [17] and the known ground-state analog mass differences tabulated in Ref. [9] for $A\leqslant59$. In the figure, all the b coefficients for a given mass number were averaged together, and error bar reflects both the standard deviation and the experimental uncertainties. Generally speaking, for a given A, the b coefficients are roughly constant, with the mean standard deviation being 61 keV. From the microscopic point of view, deviations from constancy can be expected for two reasons. First, in some cases single-particle orbits from different major oscillator shells come into play, as in $15\leqslant A\leqslant17$, and second, near the limits of stability, the single-particle orbits are nearly unbound, and the Thomas-Erhman shift [19,20] needs to be accounted for (see Sec. III).

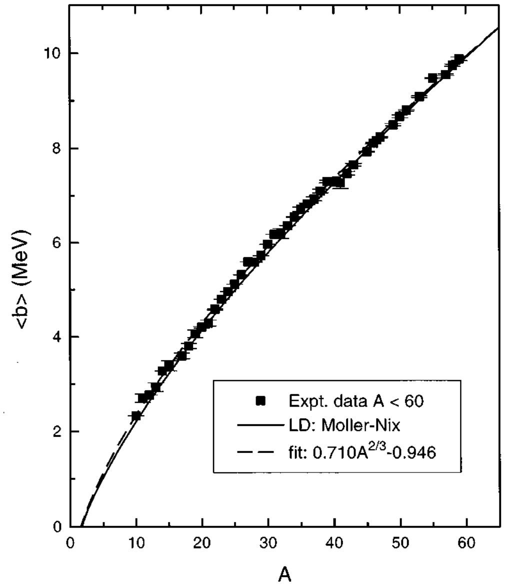

FIG. 1. Dependence of b coefficients as a function of mass number A. Experimental data are represented by the solid squares, while the values from the liquid-drop formula and the fit [Eqs. (9) and (10)] are represented by the solid and dashed lines, respectively.

From Fig. 1, it is evident that the experimental b coefficients exhibit a global $A^{2/3}$ behavior. On the other hand, Eq. (9) tends to underestimate the b coefficients for $A<40$, and the rms deviation with the data is 138 keV. Within the context of a global parametrization, a slight improvement on Eq. (9) can be obtained by fitting to the experimental data, and a rms deviation of 102 keV is achieved with

$$b=[0.710A^{2/3}-0.946]\ \mathrm{MeV}, \tag{10}$$

which is also represented in Fig. 1 by the dashed line. For the most part, Eq. (10) leads to a global description of the Coulomb energy differences between analog nuclei with an accuracy of the order $100|Z-N|$ keV. To improve upon this, it is necessary to account for local nuclear structure via a microscopic model, which is the topic of the next section.

III. SHELL-MODEL CALCULATIONS OF COULOMB ENERGY DIFFERENCES

In this section, the procedure for computing the Coulomb energy difference between analog nuclei within the framework of the shell model is outlined. In Ref. [17], empirical isovector and isotensor, or isospin-nonconserving (INC), Hamiltonians were determined for several shell-model spaces by constraining them to reproduce experimental b and c coefficients. The primary components of the empirical interactions were the Coulomb interaction and two-body isovector and isotensor interactions. In general, the empirical two-body isovector interaction was rather weak, while the isotensor interaction was found to to be consistent with the differences observed in the proton-proton and proton-neutron scattering lengths. The deviations between theoretical and experimental b and c coefficients were of the order of 30 keV and 15 keV, respectively.

In this work, proton-rich nuclei in the mass range $46 \leqslant A \leqslant 70$ are investigated. For all but two cases (the $T=1/2$, $A=69$ isodoublet and the $T=1$, $A=70$ isotriplet), the binding energy of the neutron-rich analog has been measured and is tabulated in Ref. [9]. The shell-model calculations were performed using the shell-model computer code OXBASH [21] in proton-neutron formalism using the configuration space defined by the $0f_{7/2}$, $0f_{5/2}$, $1p_{3/2}$, and $1p_{1/2}$ orbitals (the fp shell) and the FPD6 Hamiltonian given in Ref. [16]. Here, instead of computing the b coefficients, the ''Coulomb'' energy differences between analogs were computed directly by adding the INC interaction to the FPD6 Hamiltonian. Because of the large dimensions present, some truncations on the model space were found to be necessary. For $A \leqslant 59$, all configurations contained within the $0f_{7/2}$ and $1p_{3/2}$ orbits were included, and the truncations were based on the number of particles permitted to be excited out of the $0f_{7/2}$ and $1p_{3/2}$ orbits into the $0f_{5/2}$ and $1p_{1/2}$ orbits. Generally, this ranged from two to four particles so that the total dimensions (with good angular momentum) were less than 14 000. For $A > 60$, the $0f_{7/2}$ orbit was taken to be a closed core, and the $0f_{5/2}$, $1p_{3/2}$, and $1p_{1/2}$ single-particle energies of the FPD6 interaction were modified so as to reproduce the levels of ^{57}Ni under this assumption (the modified interaction is denoted as FPD6*). For the most part, it was found that the Coulomb energy shifts were not particularly sensitive to the applied truncations, and in a few cases where the effects of the truncations were tested, differences of only a few keV were found. Therefore, the applied model-space truncations are not expected to provide a significant contribution to the uncertainty in the computed binding energies.

The INC Hamiltonian used here consists of Coulomb plus nucleon-nucleon isovector and isotensor interactions. The explicit form the Hamiltonian is given in Ref. [17], and is only briefly described here. Assuming isospin to be a good quantum number in the two-nucleon system, the two-body matrix elements of the Hamiltonian may be written in terms of the $T=0$ and $T=1$ nucleon-nucleon channels as

$$H = v_{T=0} I_0^{(0)} + \sum_{k=0}^{2} v_{T=1}^{(k)} I_1^{(k)}, \tag{11}$$

where the explicit isospin dependence has been separated from the radial and spin degrees of freedom by the operators $I_T^{(k)}$ given by

$$I_0^{(0)} = \tfrac{1}{4} - \mathbf{t}(1)\cdot\mathbf{t}(2), \tag{12}$$

$$I_1^{(0)} = \tfrac{3}{4} + \mathbf{t}(1)\cdot\mathbf{t}(2), \tag{13}$$

$$I_1^{(1)} = \tfrac{1}{2}[t_z(1) + t_z(2)], \tag{14}$$

$$I_1^{(2)} = t_z(1)t_z(2) - \tfrac{1}{3}\mathbf{t}(1)\cdot\mathbf{t}(2), \tag{15}$$

with $\mathbf{t}(i)$ denoting the isospin of the ith particle. With this construction, the $T=1$ two-body matrix elements are taken to be of the form

$$V = V_0 + S_C V_C\left(\tfrac{1}{3} I_1^{(0)} + I_1^{(1)} + I_1^{(2)}\right) + S_0^{(1)} V_0 I_1^{(1)} + S_0^{(2)} V_0 I_1^{(2)}, \tag{16}$$

where V_C and V_0 represent the two-body matrix elements of the Coulomb and original isoscalar interactions, respectively. In this representation, the matrix elements of the isovector and isotensor nucleon-nucleon interactions are taken to be directly proportional to the $T=1$ matrix elements of the isoscalar Hamiltonian, i.e., the FPD6 interaction. In proton-neutron formalism, the proton-proton (pp), neutron-neutron (nn), and the $T=1$ part of the proton-neutron (pn) two-body matrix elements are given by

$$v^{(pp)} = V_0 + S_C V_C + \tfrac{1}{2} S_0^{(1)} V_0 + \tfrac{1}{6} S_0^{(2)} V_0, \tag{17}$$

$$v^{(nn)} = V_0 - \tfrac{1}{2} S_0^{(1)} V_0 + \tfrac{1}{6} S_0^{(2)} V_0, \tag{18}$$

$$v^{(pn)} = V_0 - \tfrac{1}{3} S_0^{(2)} V_0. \tag{19}$$

In addition to the two-body matrix elements in the active valence space, the effect of the INC interaction between the valence particles and the closed core must also be accounted for, and is represented by the ''Coulomb'' single-particle energies $\epsilon(\rho)$, with ρ denoting each single-particle orbit. Following Ref. [17], the ''Coulomb'' single-particle energies and the strengths of the two-body Coulomb (S_C), isovector ($S_0^{(1)}$), and isotensor ($S_0^{(2)}$) components are determined empirically by fitting to experimental b and c coefficients.

An important parameter for the INC interaction is the oscillator frequency $\hbar\omega$, since the Coulomb components are scaled as a function of A by the factor [17]

$$S(A) = \left[\frac{\hbar\omega(A)}{11.096}\right]^{1/2}. \tag{20}$$

Generally, $\hbar\omega$ is chosen to reproduce experimental rms charge radii, and for many nuclei it can be accurately parametrized by

$$\hbar\omega(A) = 45A^{-1/3} - 25A^{-2/3} \quad \text{MeV}. \tag{21}$$

It is important to note, however, that for $A \geqslant 45$, Eq. (21) underestimates $\hbar\omega$ as compared to values derived from experimental charge radii. Indeed, in Ref. [17] the value of 10.222 MeV was used for $A=53$ as opposed to the value of 10.208 MeV implied by Eq. (21). In addition, the fp-shell INC interaction was refit in Ref. [22], where it was found that better overall agreement between theoretical and experimental Coulomb energy shifts was obtained using oscillator frequencies derived from the rms charge radii of Hartree-Fock calculations using the Skyrme M^* interaction. These values of $\hbar\omega$ are tabulated in Table I, and are used in the present work.

In Refs. [17, 22], the fitted INC interactions were able to reproduce the experimental b coefficients for fp-shell nuclei with a rms deviation of approximately 33 keV. However, the most difficult parameters to determine for the INC interac-

TABLE I. Values of $\hbar\omega$ used for fp-shell nuclei.

A	$\hbar\omega$ (MeV)	A	$\hbar\omega$ (MeV)
40	10.603	60	10.156
41	10.603	61	10.087
42	10.603	62	10.017
43	10.608	63	9.954
44	10.614	64	9.890
45	10.603	65	9.786
46	10.592	66	9.681
47	10.581	67	9.589
48	10.570	68	9.496
49	10.560	69	9.460
50	10.550	70	9.424
51	10.539	72	9.331
52	10.528	73	9.168
53	10.507	74	9.203
54	10.486	76	9.032
55	10.470	77	9.100
56	10.454	78	8.923
57	10.376	79	9.869
58	10.298	80	8.816
59	10.227		

TABLE II. Comparison between theoretical (with FPD6*) and experimental excitation energies (in MeV) of the first $J^{\pi}=2^{+}$ state in even-even $N=Z$ fp-shell nuclei.

^{A}Z	Expt.	FPD6*
^{60}Zn	1.004[a]	0.825
^{64}Ge	0.902[b]	0.700
^{68}Se	0.854[b]	0.600
^{72}Kr	0.709[b]	0.707
^{76}Sr	0.261[b]	0.752
^{80}Zr	0.289[b]	-

[a] From Ref. [25]

[b] From Ref. [26]

tion are the Coulomb single-particle energies for the $0f_{5/2}$ and $1p_{1/2}$ orbits, as there is very little experimental data available that is sensitive to these quantities. In Ref. [22], these single-particle energies were fit upon by making assumptions regarding spin assignments for excited levels in ^{57}Cu and ^{59}Zn. In retrospect, these levels are probably not appropriate for determining parameters for heavier nuclei because of uncertainties in spin assignments and the fact that the levels comprising the assumed doublet at 1.040 MeV in ^{57}Cu [23] are unbound, and strong Thomas-Ehrman shifts [19,20] may apply (see below). Also, shell-model calculations for the $J^{\pi}=1/2^{-}$ and $5/2^{-}$ states in ^{59}Zn indicate that these levels are predominantly $1p_{3/2}^{3}$ configurations. On the other hand, the the beta end-point energies for both ^{62}Ga [9] and ^{66}As [24] are sensitive to the $0f_{5/2}$ Coulomb single-particle energy and were used to help fix this parameter. In regards to the $1p_{1/2}$ single-particle energy, however, no data exist that will definitively set this parameter. For this reason, the value obtained in Ref. [22], which also happens to reproduce the b coefficients for the assumed $1/2^{-}$ states in $A=57$ and 59, is used.

Two additional concerns that affect this work are (1) whether the fp shell alone is sufficient to describe the nuclei in question and (2) the effect of the Thomas-Ehrman shift on the Coulomb displacement energies near the drip line. As a measure of the appropriateness of just the fp shell for the calculations, we examine the the excitation energies of the first $J=2^{+}$ states in $N=Z$, even-even nuclei in the region $60\leqslant A\leqslant 80$. Shown in Table II, are the experimental [25,26] excitation energies of the these states in comparison with the values obtained with the FPD6* interaction (FPD6 modified as indicated above after closing the $0f_{7/2}$ orbit). Overall, there is good agreement between the calculated and experimental values until $A=76$, where there is a sudden drop in the excitation energy, which is an indication of the onset of collective behavior that would necessitate the inclusion of orbits from the next major shell, such as the $0g_{9/2}$ orbit. Given the results in Table II, the fp shell is sufficient to describe the nuclei studied in this work.

In general, Coulomb energies are computed using harmonic oscillator, or sometimes bound Woods-Saxon, single-particle wave functions for the protons, with the length scale chosen to reproduce experimental rms charge radii. Near the drip line, however, this approximation can be inadequate. Because they are loosely bound, the proton single-particle wave functions are pushed out of the nuclear interior, and as a consequence, the Coulomb energy is reduced. This shift in the Coulomb energy was first noted by Thomas [19] and Ehrman [20] in the $A=13$ system, and is most important for light nuclei where the Coulomb barrier, which acts to confine the wave function in the nuclear interior, is smaller, and for orbits with little or no centrifugal barrier, e.g., the $s_{1/2}$ orbitals. This effect is well illustrated by the single-particle states in $A=17$, where the Coulomb displacement energy of the $J^{\pi}=5/2^{+}$ (the $0d_{5/2}$ orbit) ground state is 3.543 MeV, while the shift for the $J^{\pi}=1/2^{+}$ state, which is a $1s_{1/2}$ single-particle state that is bound by only 107 keV, is 3.168 MeV. The influence of the centrifugal barrier is also apparent in these nuclei, as the Coulomb shift for the $J^{\pi}=3/2$ state (the $0d_{3/2}$ spin-orbit partner of the ground state), which is unbound by 4.5 MeV, is 3.561 MeV. On theoretical grounds, there are also self-consistent calculations [27] that suggest that Thomas-Ehrman shifts for nuclei near the drip line may be as large a few hundred keV. Because of the empirical nature of the INC interaction, however, it is not clear how much of the Thomas-Ehrman effect has been absorbed into the interaction by the fit. In addition, for nuclei near the drip line, the estimate of the theoretical uncertainty is of the order of 100–250 keV, and the effects of the Thomas-Ehrman shift are likely to lie within the quoted uncertainties for the absolute binding energy.

The parameters for the INC interaction used in this work are $\epsilon(0f_{7/2})=7.487$ MeV, $\epsilon(1p_{3/2})=7.312$ MeV, $\epsilon(0f_{5/2})=7.337$ MeV, $\epsilon(1p_{1/2})=7.240$ MeV, $S_{C}=1.006$, $S_{0}^{(1)}=0.0$, and $S_{0}^{(2)}=-4.2\times 10^{-2}$. Last, because of the difficulties associated with determining the $0f_{5/2}$ and $1p_{3/2}$ single-particle energies, the uncertainties in the theoretical estimates of the b coefficients for nuclei with $A>60$ are increased from 33 keV to 45 keV.

Shown in Table III are the results obtained for proton-rich nuclei whose binding energies are unknown in the mass re-

TABLE III. Predicted binding energies, one- and two-proton separation energies (S_p and S_{2p}, respectively), and β-decay end-point energies for proton rich nuclei with $46 \leqslant A \leqslant 70$. The absolute binding energies were computed with theoretical Coulomb energy shifts added onto the experimental binding energy for the neutron-rich analog, also listed in the table.

^{A}Z	T_z	J^{π}	$\mathrm{BE}_{\mathrm{theory}}$ (MeV)	^{A}Z-analog	$\mathrm{BE}_{\mathrm{expt}}^{\mathrm{analog}}$ (MeV)	S_p (MeV)	S_{2p} (MeV)	Q_{EC} (MeV)
^{46}Mn	2	4^+	364.186(132)	^{46}Sc	396.610(1)	0.156(146)	3.234(139)	17.007(134)
^{46}Fe	3	0^+	350.144(198)	^{46}Ca	398.769(2)	1.408(224)	0.328(215)	13.260(238)
^{47}Mn	3/2	$5/2^-$	382.326(99)	^{47}Ti	407.072(1)	0.351(101)	5.237(100)	12.020(100)
^{47}Fe	5/2	$7/2^-$	365.973(165)	^{47}Sc	407.254(2)	1.787(211)	1.943(177)	15.571(192)
^{47}Co	7/2	$7/2^-$	348.349(231)	^{47}Ca	406.045(2)	−1.795(304)	−0.387(254)	-
^{48}Mn	1	4^+	397.101(66)	^{48}V	413.904(3)	1.973(68)	6.740(66)	13.579(66)
^{48}Fe	2	0^+	385.106(132)	^{48}Ti	418.698(1)	2.780(165)	3.131(134)	11.213(148)
^{48}Co	3	6^+	365.153(198)	^{48}Sc	415.487(5)	−0.820(258)	0.967(238)	-
^{48}Ni	4	0^+	348.854(264)	^{48}Ca	415.991(4)	0.505(351)	−1.290(330)	15.517(330)
^{49}Fe	3/2	$7/2^-$	399.802(99)	^{49}V	425.457(1)	2.701(119)	4.674(100)	12.963(102)
^{49}Co	5/2	$7/2^-$	384.184(165)	^{49}Ti	426.841(1)	−0.922(211)	1.858(192)	-
^{49}Ni	7/2	$7/2^-$	365.830(231)	^{49}Sc	425.618(4)	0.677(304)	−0.143(284)	17.572(284)
^{49}Cu	9/2	$3/2^-$	344.413(297)	^{49}Ca	421.138(4)	−4.441(397)	−3.936(376)	-
^{50}Co	2	6^+	400.060(132)	^{50}V	434.790(1)	0.258(165)	2.959(148)	16.585(145)
^{50}Ni	3	0^+	385.693(198)	^{50}Ti	437.780(1)	1.509(258)	0.587(238)	13.585(238)
^{50}Cu	4	5^+	362.299(264)	^{50}Sc	431.674(16)	-3.531(351)	-2.854(330)	-
^{50}Zn	5	0^+	340.823(330)	^{50}Ca	427.491(9)	−3.590(444)	−8.031(423)	-
^{51}Co	3/2	$7/2^-$	417.864(99)	^{51}Cr	444.306(1)	0.164(116)	4.317(102)	12.868(100)
^{51}Ni	5/2	$7/2^-$	401.684(165)	^{51}V	445.841(1)	1.624(211)	1.882(192)	15.398(192)
^{51}Cu	7/2	$3/2^-$	382.472(231)	^{51}Ti	444.153(1)	−3.221(304)	−1.712(284)	-
^{52}Co	1	6^+	432.912(66)	^{52}Mn	450.851(2)	1.398(68)	6.283(66)	14.003(67)
^{52}Ni	2	0^+	420.478(132)	^{52}Cr	456.345(1)	2.614(165)	2.778(145)	11.652(148)
^{52}Cu	3	3^+	399.399(198)	^{52}V	453.152(1)	−2.285(258)	−0.661(238)	-
^{52}Zn	4	0^+	380.321(264)	^{52}Ti	451.961(7)	−2.151(351)	−5.372(330)	-
^{53}Ni	3/2	$7/2^-$	435.558(99)	^{53}Mn	462.905(2)	2.646(119)	4.044(100)	12.956(101)
^{53}Cu	5/2	$3/2^-$	418.835(165)	^{53}Cr	464.285(2)	−1.643(211)	0.971(192)	-
^{53}Zn	7/2	$7/2^-$	397.948(231)	^{53}V	461.631(3)	−1.451(304)	−3.736(284)	-
^{54}Cu	2	3^+	434.906(132)	^{54}Mn	471.844(2)	−0.652(165)	1.994(148)	-
^{54}Zn	3	0^+	418.605(198)	^{54}Cr	474.004(1)	−0.230(258)	−1.873(238)	15.519(238)
^{54}Ga	4	3^+	393.891(264)	^{54}V	467.744(15)	−4.057(351)	−5.508(330)	-
^{55}Cu	3/2	$3/2^-$	452.997(99)	^{55}Fe	481.057(1)	−0.153(111)	3.701(101)	13.568(100)
^{55}Zn	5/2	$5/2^-$	435.071(165)	^{55}Mn	482.071(1)	0.165(211)	−0.487(192)	17.144(192)
^{55}Ga	7/2	$3/2^-$	414.644(231)	^{55}Cr	480.250(1)	−3.961(304)	−4.191(284)	-
^{56}Cu	1	4^+	467.899(66)	^{56}Co	486.906(1)	0.552(67)	5.166(66)	15.307(67)
^{56}Zn	2	0^+	454.214(132)	^{56}Fe	492.254(1)	1.217(165)	1.064(141)	12.903(148)
^{56}Ga	3	3^+	432.226(198)	^{56}Mn	489.315(1)	−2.845(258)	−2.680(238)	-
^{56}Ge	4	0^+	412.381(264)	^{56}Cr	488.507(10)	−2.263(351)	−6.224(330)	-
^{57}Zn	3/2	$7/2^-$	469.440(99)	^{57}Co	498.282(1)	1.541(119)	2.093(100)	14.461(100)
^{57}Ga	5/2	$3/2^-$	451.874(165)	^{57}Fe	499.885(1)	−2.340(211)	−1.123(192)	-
^{57}Ge	7/2	$5/2^-$	430.634(231)	^{57}Mn	497.992(3)	−1.592(304)	−4.437(284)	-
^{58}Ga	2	2^+	468.039(132)	^{58}Co	506.855(2)	−1.401(165)	0.140(148)	-
^{58}Ge	3	0^+	451.578(198)	^{58}Fe	509.945(1)	−0.296(258)	−2.636(238)	15.679(238)
^{58}As	4	3^+	426.697(266)	^{58}Mn	504.480(30)	−3.937(352)	−5.529(331)	-
^{59}Ga	3/2	$3/2^-$	486.040(99)	^{59}Ni	515.453(1)	−0.920(111)	1.357(100)	-
^{59}Ge	5/2	$7/2^-$	468.097(165)	^{59}Co	517.308(1)	0.058(211)	−1.343(192)	17.161(192)
^{59}As	7/2	$3/2^-$	447.648(231)	^{59}Fe	516.526(1)	−3.930(304)	−4.226(284)	-
^{60}Ga	1	2^+	500.080(66)	^{60}Cu	519.933(3)	0.080(77)	2.971(66)	14.130(67)
^{60}Ge	2	0^+	487.127(132)	^{60}Ni	526.842(1)	1.087(165)	0.167(141)	12.171(148)
^{60}As	3	5^+	465.094(198)	^{60}Co	524.800(1)	−3.003(258)	−2.945(238)	-
^{61}Ga	1/2	$3/2^-$	515.179(48)	^{61}Zn	525.223(16)	0.187(49)	5.307(48)	9.262(50)
^{61}Ge	3/2	$3/2^-$	501.415(135)	^{61}Cu	531.642(2)	1.335(150)	1.415(141)	12.982(143)
^{61}As	5/2	$3/2^-$	484.381(225)	^{61}Ni	534.595(1)	−2.746(261)	−1.659(246)	-

TABLE III. (*Continued*).

^{A}Z	T_z	J^{π}	BE_{theory} (MeV)	^{A}Z-analog	BE^{analog}_{expt} (MeV)	S_p (MeV)	S_{2p} (MeV)	Q_{EC} (MeV)
^{62}Ge	1	0^+	517.720(91)	^{62}Zn	538.119(10)	2.541(102)	2.728(91)	9.664(95)
^{62}As	2	1^+	499.816(180)	^{62}Cu	540.529(4)	−1.599(225)	−0.264(192)	-
^{62}Se	3	0^+	484.239(270)	^{62}Ni	545.259(1)	−0.142(351)	−2.888(301)	14.795(325)
^{63}Ge	1/2	$3/2^-$	530.597(110)	^{63}Ga	540.930(100)	2.431(113)	5.374(111)	9.551(148)
^{63}As	3/2	$3/2^-$	516.321(135)	^{63}Zn	547.232(2)	−1.399(163)	1.142(143)	-
^{63}Se	5/2	$3/2^-$	499.885(225)	^{63}Cu	551.382(1)	0.069(288)	−1.530(262)	15.654(262)
^{64}As	1	0^+	530.315(90)	^{64}Ga	551.147(4)	−0.282(142)	2.149(94)	14.853(266)
^{64}Se	2	0^+	517.411(180)	^{64}Zn	559.094(2)	1.090(225)	−0.309(202)	12.122(201)
^{65}As	1/2	$3/2^-$	545.522(46)	^{65}Ge	556.010(10)	−0.428(254)	4.592(110)	-
^{65}Se	3/2	$3/2^-$	531.473(135)	^{65}Ga	563.036(2)	1.158(162)	0.876(174)	13.267(143)
^{65}Br	5/2	$1/2^-$	514.580(225)	^{65}Zn	567.020(2)	−2.831(288)	−1.741(262)	-
^{66}Se	1	0^+	548.091(95)	^{66}Ge	569.290(30)	2.569(105)	2.141(267)	10.087(112)
^{66}Br	2	0^+	529.780(180)	^{66}Ga	572.176(3)	−1.693(225)	−0.535(201)	-
^{66}Kr	3	0^+	514.579(270)	^{66}Zn	578.133(2)	−0.001(351)	−2.832(325)	14.419(325)
^{67}Se	1/2	$5/2^-$	560.882(110)	^{67}As	571.610(100)	1.922(125)	4.872(110)	-
^{67}Br	3/2	$1/2^-$	546.355(135)	^{67}Ge	578.398(5)	−1.736(165)	0.833(143)	-
^{67}Kr	5/2	$1/2^-$	529.935(225)	^{67}Ga	583.403(2)	0.155(288)	−1.538(262)	15.638(262)
^{68}Br	1	3^+	560.365(135)	^{68}As	581.910(100)	−0.517(174)	1.405(147)	-
^{68}Kr	2	0^+	547.668(180)	^{68}Ge	590.792(6)	1.313(225)	−0.423(204)	11.915(225)
^{68}Rb	3	1^+	526.980(270)	^{68}Ga	591.680(2)	−2.955(351)	−2.800(325)	-
^{69}Br	1/2	$3/2^-$	575.737(54)	^{69}Se	586.620(30)	−0.663(305)	4.127(114)	-
^{69}Kr	3/2	$5/2^-$	561.477(138)	^{69}As	594.180(30)	0.075(193)	−0.442(176)	14.515(148)
^{70}Rb	2	4^+	559.398(187)	^{70}As	603.520(50)	−1.042(232)	−0.967(230)	-

gion $46 \leqslant A \leqslant 69$. The table lists the experimental binding energy of the neutron-rich analog, the predicted binding energy, and one- and two-proton separation energies, as well as the Q value for electron capture (Q_{EC}). The ground-state spins were taken from Ref. [25] and are also listed in the table. Wherever available, experimental binding energies tabulated in Ref. [9] were used in conjunction with theoretical values to compute Q_{EC} and the separation energies.

In addition to the nuclei listed in Table III, predictions for the ''Coulomb'' energy differences for the the $T=1/2$, $A=69$ isodoublet and the $T=1$, $A=70$ isotriplet, for which the binding energy of the neutron-rich member has not yet been measured experimentally, are given in Table IV. The theoretical uncertainties for $A=70$ include an uncertainty of 20 keV in the c coefficient of Eq. (1).

Shown in Fig. 2 is a comparison of the binding energies reported here with those from three other theoretical studies. This comparison is illustrated by the difference $\Delta BE = BE(\text{this work}) - BE(\text{other work})$, which is plotted in the figure as a function of mass number, with the ordering the same as in Table III. The error bars plotted at $\Delta BE=0$ represent the theoretical uncertainty of the binding energies listed in Table III. The open circles show the comparison with the previous shell-model calculations of Ormand in Ref. [7] ($A \leqslant 48$) and the open triangles the comparison with the binding energies of Cole in Ref. [8] ($A \leqslant 52$), while the solid squares represent the comparison with the binding energies obtained from the unified macroscopic-microscopic model of

TABLE IV. Predictions for the ''Coulomb'' energy difference for the $T=1/2$, $A=69$ and $T=1$, $A=70$ nuclei.

$^{Z}A - ^{Z-1}A$	J^{π}	ΔBE (MeV)
^{69}Br-^{69}Se	$3/2^-$	−10.883(45)
^{70}Kr-^{70}Br	0^+	−11.241(50)
^{70}Br-^{70}Se	0^+	−10.801(50)

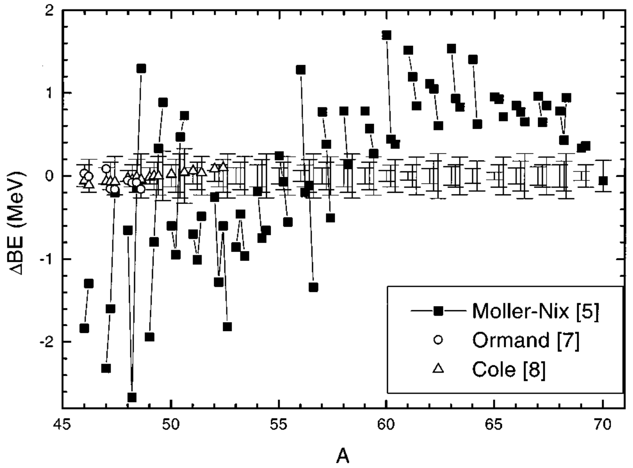

FIG. 2. Difference between absolute binding energies listed in Table III with those of Möller and Nix [5] (solid squares), Ormand [7], and Cole [8] (open triangles). The error bars at $\Delta BE=0$ denote the theoretical uncertainty of the binding energies listed in Table III.

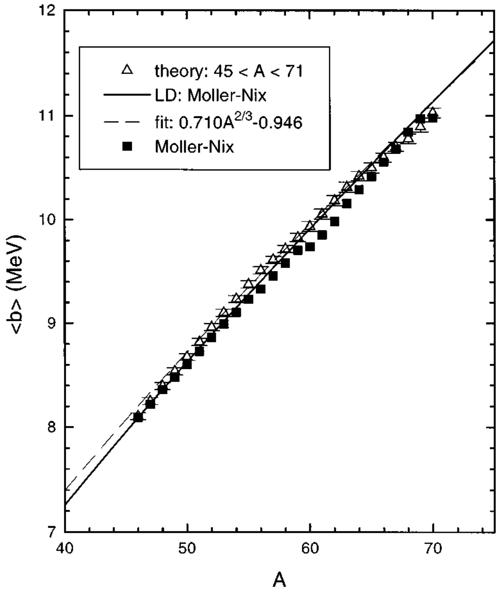

FIG. 3. Dependence of theoretical b coefficients for nuclei listed in Table III (open triangles) as a function of mass number A. For comparison, the b coefficients derived from the unified microscopic-macroscopic model of Möller and Nix [5] are also shown (solid squares). The systematic behavior as expected from Eqs. (9) and (10) is represented by the solid and dashed lines, respectively.

Möller and Nix [5] $(46 \leqslant A \leqslant 70)$. While the results of Refs. [7, 8] are in agreement with those reported here, those of Möller and Nix are in severe disagreement for some nuclei. The origin of these differences is twofold. First, in the Möller-Nix study, the Coulomb energy difference between analog nuclei is considerably smaller than in this work. This is illustrated in Fig. 3, where the b coefficients for the nuclei listed in Table III (open triangles) are plotted as a function of A in comparison with those derived from the Möller-Nix masses (solid squares). In the mass region $52 \leqslant A \leqslant 64$ the Möller-Nix b coefficients are generally 100–200 keV smaller than those determined here. In addition, the Möller-Nix b coefficients are also in disagreement experimental trends, as is evidenced by the ^{59}Zn-^{59}Cu binding energy differences, where the Möller-Nix b coefficient is 9.683 MeV, which is 200 keV smaller than the experimental value of 9.881(40) MeV [9]. The second reason for the large disagreement in Fig. 2 can be attributed to poor reproduction of the mass of the neutron-rich analog nucleus. For example, the Möller-Nix ^{59}Cu mass excess is -54.8 MeV, which is in considerable disagreement with the experimental value of $-56.3515(17)$ MeV tabulated in Ref. [9].

Also shown in Fig. 3 is a comparison between the theoretical b coefficients and the systematic trends expected from the liquid-drop model of Eq. (9) (solid line) and the fit of Eq. (10) (dashed line). For the most part, the shell-model b coefficients derived from the nuclei listed in Table III are in good agreement with the fitted parametrization of Eq. (10), although they tend to be somewhat smaller than the systematic trend in the regions $A<50$ and $A>66$. Note that for $A<50$, this is a continuation of the trend for experimental data as is observed in Fig. 1 for $40 \leqslant A \leqslant 50$.

TABLE V. Comparison between experimental and predicted beta-decay half-lives for odd-odd, $N=Z$ Fermi transitions. The predicted Q_{EC}-value is also given.

^{Z}A	Q_{EC} (MeV)	$t_{1/2}$ (ms)	$t_{1/2}^{\mathrm{expt}}$ (ms)
^{62}Ga	9.191(50)	115(2)	116.1(2)[a]
^{66}As	9.592(50)	94(2)	95.8(2)[b]
^{70}Br	10.019(50)	76(3)	79.1(8)[c]

[a] From Ref. [29].
[b] From Ref. [24].
[c] From Ref. [30].

As a further illustration of the systematic trend for the Coulomb energy shifts, we examine the half-lives for the Fermi transition between analog $J^{\pi}=0^{+}$, $T=1$ states in $N=Z$, odd-odd nuclei with $A=62$, 66, and 70. The partial half-life for the β decay from the parent ground state to the ith state in daughter nucleus is given by

$$t_{1/2}^{i}=\frac{K}{G_{V}^{2}|\mathcal{M}_{o\rightarrow i}|^{2}f_{o\rightarrow i}}, \tag{22}$$

where $K=2\pi^{3}(\ln 2)\hbar^{7}/(m_{e}^{5}c^{4})$ and $K/G_{V}^{2}=6170\pm4$ s [28]. The statistical rate function $f_{o\rightarrow i}$ depends on the beta end-point energy and here it is evaluated using Eq. (10) of Ref. [7]. For a pure Fermi transition between $T=1$ analog states, the transition matrix element $\mathcal{M}_{o\rightarrow i}$ is given by $\sqrt{2(1-\delta_{C})}$, where δ_{C} is a small correction due to isospin-symmetry breaking. Recent calculations [22] indicate that for these nuclei δ_{C} is expected to be of the order 1–2 %, and for the purpose of comparing with experimental data, will be taken to be equal to 1.5%. In general, Gamow-Teller transitions to excited states may also take place, and would tend to decrease the total beta-decay half-life. However, not only are the matrix elements for these transitions much smaller than for the Fermi transition, but since they occur to states in the daughter nucleus at a higher excitation energy, the statistical rate function is also much smaller. Hence, to a good approximation, the beta decay of these nuclei may be taken to be pure Fermi. Listed in Table V are the predicted Q values for electron capture as well as a comparison between the experimental [24,29,30] and predicted beta-decay half-lives. Given the fact that the statistical rate function strongly depends on the beta end-point energy (to the fifth power), the excellent agreement between the experimental and predicted beta-decay half-lives for all three nuclei is a good indication that the overall systematic behavior of the Coulomb energy differences is well reproduced here.

This section is concluded with a discussion on ^{65}As, which is important from an astrophysical point of view. Because of the long beta-decay half-life for ^{64}Ge, if ^{65}As were significantly proton unbound, ^{64}Ge would then become a ‘‘waiting point’’ in the rp process and would inhibit the production of heavier elements. If, however, the half-life of ^{65}As is dominated by beta decay, the rp process will proceed through ^{65}As primarily by proton capture to ^{66}Se, although photodisintegration may begin to play an important role if ^{65}As is proton unbound [31].

From Table III, ^{65}As is found in this work to be unbound to proton emission by 0.428(254) MeV, with most of the uncertainty due to the uncertainty in the binding energy for ^{64}Ge (0.250 MeV). On the other hand, ^{65}As has been observed experimentally [32] with a beta-decay half-life of 190^{+110}_{-70} ms. From the fact that no protons were observed in the stopping detector during this experiment, it may be inferred that the partial half-life for proton emission is significantly longer and must be greater than 1 s. The partial half-life for proton emission may be estimated using the WKB approximation, which is outlined in some detail in the next section [see Eq. (23)] and, in particular for proton emission, in Ref. [33]. A shell-model calculation within the fp shell assuming a closed $0f_{7/2}$ orbit and the FPD6* interaction yields 0.13 for the spectroscopic factor θ^2. Using the potential parameters of Ref. [33], a partial half-life for proton emission longer than 1 s requires the one-proton separation energy to be greater than -0.23 MeV, which is in agreement with the value given in Table III. Because of the extreme sensitivity on the separation energy, however, it may never be possible to give a reasonable prediction for the partial half-life for proton emission without explicitly measuring the masses for both ^{64}Ge and ^{65}As. With the present uncertainty of 0.254 MeV, a range of 16 orders of magnitude is found for the half-life, i.e., between 1.4×10^{-12} and 1.6×10^{4} s. On the other hand, supposing that the binding energy of ^{64}Ge could be measured to within a few keV, a theoretical uncertainty of $\sim$50 keV remains for ^{65}As, which for a separation energy of -0.2 MeV leads to a range of nearly four orders of magnitude in the proton partial half-life.

IV. IDENTIFICATION OF CANDIDATES FOR DIPROTON EMISSION

In this section, the partial half-lives for diproton emission are examined, with the intention of identifying candidates amenable to experimental detection while taking into account theoretical uncertainties. As was mentioned in the introduction, the range of observable lifetimes for diproton emission is limited by competing decay mechanisms and experimental setups. In general, all candidates for diproton emission have large β end points, and as a consequence, the β-decay half-lives are expected to be of the order of 1–100 ms [7]. Also, in several experiments, such as in Ref. [3], the initial nucleus must live long enough to be identified. In this case, the limiting time is determined by the time of flight in the experimental apparatus. In general, these two conditions impose a practical limit on the observable half-life for diproton emission to be in the range $10^{-8}-10^{-3}$ s.

In Refs. [6, 7], the diproton decay half-lives were estimated using r-matrix theory [34] while taking the channel radius R_0 to be 4 fm for all cases. In contrast, in Ref. [27] the half-life for ^{48}Ni was estimated using the Wentzel-Kramers-Brillouin (WKB) approximation. Because of uncertainties associated with the choice of the channel radius, the WKB approximation for the diproton decay half-life will be used here. Following Ref. [27], the WKB expression for the partial decay width is

$$\Gamma_{2p}=\theta^2\mathcal{N}\frac{\hbar^2}{4\mu}\exp\left[-2\int_{r_{\rm in}}^{r_{\rm out}}dr\,k(r)\right], \qquad (23)$$

where θ^2 is the spectroscopic factor for finding the diproton in the correlated $L=0$ state, μ is the reduced mass, $r_{\rm in}$ and $r_{\rm out}$ are the classical inner and outer turning points, respectively, the normalization factor $\mathcal{N}$ is determined by

$$\mathcal{N}\int_0^{r_{\rm in}}dr\,\frac{1}{k(r)}\cos^2\left[\int_0^{r}dr'\,k(r')-\frac{\pi}{4}\right]=1, \qquad (24)$$

and $k(r)$ is the wave number given by

$$k(r)=\sqrt{\frac{2\mu}{\hbar^2}\frac{m^*(r)}{m}\,|Q_{2p}-V_{2p}(r)|}. \qquad (25)$$

In Eq. (25), the asymptotic energy of the diproton is $Q_{2p}=-S_{2p}$, $V_{2p}(r)$ is the average diproton potential, and $m^*(r)/m$ is the proton effective mass. As in Ref. [27], $V_{2p}(r)$ is approximated by $2V_p(r)$, where $V_p(r)$ is the self-consistent proton potential for the $(Z-2,N)$ nucleus obtained from a Hartree-Fock or a Hartree-Fock-Bogoliubov calculation. Here, the half-lives were computed using Hartree-Fock potentials using a Skyrme-type two-body interaction. It was found that the various Skyrme interactions give half-lives that are in agreement to within a factor of 2, and the results reported here were obtained using the Skyrme M^* interaction. In addition, the half-lives computed using Eq. (23) were found to be approximately an order of magnitude shorter than those obtained using the r-matrix representation with $R_0=4$ fm (as was used in Refs. [6, 7]). On the other hand, if the channel radius is chosen to be equal to the classical inner turning point, $r_{\rm in}$, the r-matrix approach yields half-lives that are within a factor of 2 of the WKB method.

The spectroscopic factor θ can be evaluated within the framework of the shell model. For diproton emission the spectroscopic factor can be estimated using the cluster-overlap approximation [35], namely,

$$\theta^2=G^2[A/(A-k)]^{\lambda}|\langle\Psi_f|\psi_c|\Psi_i\rangle|^2, \qquad (26)$$

where k, λ, and G^2 are parameters dependent on the model space and the emitted cluster, and ψ_c is a two-proton cluster wave function in which the relative motion of the particles is governed by the $0S$ state, and is obtained by diagonalizing an SU(3)-conserving interaction within the shell-model configuration space [35].

Of all the quantities in Eq. (23), the diproton decay rate is most sensitive to the two-proton separation energy S_{2p}. Indeed, it was illustrated in Ref. [7] that an uncertainty of ±100 keV in a separation energy of the order 500 keV can lead to a range of nearly six orders of magnitude in the diproton decay half-life. In contrast, the spectroscopic factors are expected to be of the order of 0.5–0.75 [6], and should not lead to any more than an order-of-magnitude decrease in the decay rate (increase in the half-life). Given that the theoretical uncertainties in the separation energy for each of the diproton emitters considered in this work are all greater than 175 keV, an accurate estimate of the spectroscopic factor is not needed in order to obtain an order-of-magnitude estimate of the diproton half-life for the purpose of identifying the best candidates for experimental observation. Hence, the life-

TABLE VI. Half-lives for diproton emitter candidates. Also listed are the theoretical predictions for the one- and two-proton separation energies.

${}^{A}Z$	S_p (MeV)	S_{2p} (MeV)	$t_{1/2}$ (s)	$t_{1/2}^{\min}$ (s)	$t_{1/2}^{\max}$ (s)
		Ref. [7]			
^{38}Ti	0.438(164)	$-2.432(132)$	9×10^{-16}	4×10^{-16}	2×10^{-15}
^{45}Fe	$-0.010(198)$	$-1.279(181)$	10^{-6}	10^{-8}	10^{-4}
^{48}Ni	0.502(164)	$-1.137(210)$	3×10^{-3}	10^{-5}	4
		This work			
^{48}Ni	0.505(351)	$-1.290(330)$	4×10^{-6}	5×10^{-9}	0.09
^{49}Ni	0.677(304)	$-0.143(284)$	3×10^{49}	6×10^{14}	∞
^{55}Zn	0.165(211)	$-0.487(192)$	5×10^{14}	2×10^{9}	3×10^{30}
^{59}Ge	0.058(211)	$-1.343(192)$	10^{-3}	10^{-5}	0.3
^{63}Se	0.069(288)	$-1.530(262)$	6×10^{-5}	3×10^{-7}	5×10^{-2}
^{64}Se	1.090(225)	$-0.309(202)$	5×10^{32}	6×10^{17}	4×10^{79}
^{66}Kr	$-0.001(351)$	$-2.832(325)$	3×10^{-12}	2×10^{-13}	6×10^{-11}
^{67}Kr	0.155(288)	$-1.538(262)$	2×10^{-3}	10^{-5}	0.2
^{68}Kr	1.313(225)	$-0.423(204)$	3×10^{24}	8×10^{13}	5×10^{49}
^{69}Kr	0.075(193)	$-0.442(176)$	2×10^{23}	2×10^{14}	10^{40}

times reported here are evaluated assuming $\theta^2=1$ with the understanding that they are probably too short by a factor of 2–4.

Listed in Table VI are the half-lives ($t_{1/2}=\hbar\ \ln 2/\Gamma_{2p}$) associated with diproton emission for all nuclei in Table III that are predicted to be unstable to two-proton emission while being bound to proton emission. Also, for the purpose of comparison, the half-lives for ^{38}Ti, ^{45}Fe, and ^{48}Ni given in Ref. [7] are also listed in the table. Given the practical limitations on the half-life for the experimental observation of this decay mode, the best candidates are ^{45}Fe, ^{48}Ni, and ^{63}Se. Of these three, perhaps the best is ^{45}Fe since it is likely that it has already been identified experimentally [3]. On the other hand, both ^{59}Ge and ^{67}Kr have half-lives that are long enough to make them marginal candidates for experimental observation.

V. CONCLUSIONS

In this work, Coulomb energy differences between mirror nuclei with $46\leqslant A\leqslant 70$ were computed within the framework of the nuclear shell model using an effective Coulomb plus isotensor interaction. Absolute binding energies for proton-rich nuclei are predicted by adding the Coulomb energy differences to the experimental binding energy of the neutron-rich analog. With these binding energies, proton separation energies are computed, and the location of the proton drip line is delineated.

The computed Coulomb energy differences were also compared with systematic trends predicted by the liquid-drop model and a fit to experimental b coefficients assuming a $A^{2/3}$ dependence. It was found that the shell-model calculations were in good agreement with the systematic trends, except for $A\leqslant 50$ and $A\geqslant 66$. As a further test on the systematic trend of the shell-model Coulomb shifts, half-lives for the Fermi transitions in odd-odd, $N=Z$ nuclei with $A=62$, 66, and 70 were computed and found to be in excellent agreement with experimental data. The shell-model binding energies predicted here were also compared with three previous works. While the results of Ormand [7] (only for $A\leqslant 48$) and Cole [8] (only for $A\leqslant 52$) are in good agreement with those reported here, those of Möller and Nix [5] are not. It was found that the disagreement with the Möller-Nix masses is due to differences in both the Coulomb energy shifts and the binding energy of the neutron-rich analog. For the most part, the data presented in Fig. 1 are the only data that are explicitly sensitive to a parametrization of the Coulomb energy. Given the importance of analog symmetry and the overall success of the IMME, any global parametrization of binding energies should include a proper description of the Coulomb energy differences. Towards this end, perhaps the best approach is to determine the parameters of a microscopic-macroscopic model using the neutron-rich binding energies, while fixing the parameters of the Coulomb plus isovector part so as to reproduce the Coulomb energy shifts between mirror nuclei. Even in this limit, however, it has to be noted that the systematic parametrization is capable of reproducing the experimental b coefficients of the IMME only at the level of approximately 100 keV.

Finally, two-proton separation energies were also computed, and half-lives associated with correlated diproton emission were computed using the WKB approximation. Given practical constraints on the half-life for the observation of this decay mode imposed by competition with beta decay and experimental setups, the best candidates for experimental observation are predicted to be ^{45}Fe, ^{48}Ni, and ^{63}Se.

ACKNOWLEDGMENTS

Discussions with B. A. Brown, W. Nazarewicz, and M. Thoennessen are gratefully acknowledged. Oak Ridge National Laboratory is managed for the U.S. Department of Energy by Lockheed Martin Energy Research Corp. under Contract No. DE-AC05-96OR22464. This work was supported in part by NSF Cooperative Agreement No. EPS 9550481, NSF Grant No. 9603006, and U.S. DOE Contract No. DE-FG02-96ER40985.

[1] E. M. Burbidge, G. R. Burbidge, W. A. Fowler, and F. Hoyle, Rev. Mod. Phys. **29**, 547 (1957).

[2] R. K. Wallace and S. E. Woosley, Astrophys. J. Suppl. **45**, 389 (1981).

[3] B. Blank *et al.*, Phys. Rev. Lett. **77**, 2893 (1996).

[4] P. Möller, W. D. Myers, W. J. Swiatecki, and J. Treiner, At. Data Nucl. Data Tables **39**, 225 (1988). F. Buchinger *et al.*, Phys. Rev. C **49**, 1402 (1994); P. Möller, J. R. Nix, W. D. Myers, and W. J. Swiatecki, At. Data Nucl. Data Tables **59**, 185 (1995).

[5] P. Möller and J. R. Nix, At. Data Nucl. Data Tables **39**, 213 (1988).

[6] B. A. Brown, Phys. Rev. C **43**, R1513 (1991).

[7] W. E. Ormand, Phys. Rev. C **53**, 214 (1996).

[8] B. J. Cole, Phys. Rev. C **54**, 1240 (1996).

[9] G. Audi and A. H. Wapstra, Nucl. Phys. **A565**, 1 (1993).

[10] E. P. Wigner, in *Proceedings of the Robert A. Welsch Conference on Chemical Research*, edited by W. D. Milligan (R. A. Welsch Foundation, Houston, TX, 1958), Vol. 1, p. 88.

[11] W. Benenson and E. Kashy, Rev. Mod. Phys. **51**, 527 (1979).

[12] Assuming only two-body interactions, the IMME is exact at the level of first-order perturbation theory. At present, the only known exception to the IMME is the $J^{\pi}=3/2^{-}, T=3/2$ multiplet for $A=9$ [11].

[13] Strictly speaking, the a coefficient contains a small part due to the isotensor interaction. See Eq. (2.5a) in Ref. [17].

[14] B. H. Wildenthal, in *Progress in Particle and Nuclear Physics*, edited by D. H. Wilkinson (Pergamon, Oxford, 1984), Vol. 11, p. 5.

[15] E. K. Warburton, J. A. Becker, and B. A. Brown, Phys. Rev. C **41**, 1147 (1990).

[16] W. A. Richter, M. G. van der Merwe, R. E. Julies, and B. A. Brown, Nucl. Phys. **A523**, 325 (1990).

[17] W. E. Ormand and B. A. Brown, Nucl. Phys. **A491**, 1 (1989).

[18] B. J. Cole, J. Phys. G **11**, 351 (1985); **14**, 37 (1988).

[19] R. F. Thomas, Phys. Rev. **81**, 148 (1951); **88**, 1109 (1952).

[20] J. B. Ehrman, Phys. Rev. **81**, 412 (1951).

[21] B. A. Brown, A. Etchegoyen, and W. D. M. Rae, the Oxford University-Buenos Aires-MSU shell model code OXBASH, Michigan State University Cyclotron Laboratory Report No. 524, 1985.

[22] W. E. Ormand and B. A. Brown, Phys. Rev. C **52**, 2455 (1995).

[23] M. R. Bhat, Nucl. Data Sheets **67**, 195 (1992).

[24] M. R. Bhat, Nucl. Data Sheets **61**, 461 (1990).

[25] *Table of Isotopes*, edited by R. B. Firestone and V. S. Shirley, 8th edition (Wiley & Sons, New York, 1996).

[26] C. J. Lister *et al.*, in *Nuclei far from Stability: Fifth International Conference*, ed. by Ian S. Towner, AIP Conf. Proc. 164 (AIP, New York, 1987), p. 354.

[27] W. Nazarewicz *et al.*, Phys. Rev. C **53**, 740 (1996).

[28] D. H. Wilkinson, A. Gallman, and D. E. Alburger, Phys. Rev. C **18**, 401 (1978).

[29] M. M. King, Nucl. Data Sheets **60**, 337 (1990).

[30] M. R. Bhat, Nucl. Data Sheets **68**, 117 (1993).

[31] A. E. Champagne and M. Wiescher, Annu. Rev. Nucl. Part. Sci. **42**, (1992).

[32] J. A. Winger *et al.*, Phys. Lett. B **299**, 214 (1993).

[33] S. Hofmann, in *Particle Emission from Nuclei, Vol. II*, edited by D. N. Poenaru and M. S. Evasçu (CRC Press, Boca Raton, FL, 1989), p. 25; S. Hofmann (unpublished).

[34] A. M. Lane and R. G. Thomas, Rev. Mod. Phys. **30**, 257 (1958); M. H. Macfarlane and J. B. French, *ibid.* **32**, 567 (1960).

[35] W. Chung, J. van Hienen, B. H. Wildenthal, and C. L. Bennett, Phys. Lett. **79B**, 381 (1978); J. B. McGrory, *ibid.* **47B**, 481 (1973); M. Ichimura, A. Arima, E. C. Halbert, and T. Terasawa, Nucl. Phys. **A204**, 225 (1973).